npj computational materials

www.nature.com/npjcompumats

ARTICLE OPEN

Check for updates

Resonant tunneling in disordered borophene nanoribbons with line defects

Pei-Jia Hu[1], Si-Xian Wang[1], Xiao-Feng Chen[1,2], Zeng-Ren Liang[1], Tie-Feng Fang[3], Ai-Min Guo[1]✉, Hui Xu[1] and Qing-Feng Sun[4,5,6]

Recently, borophene has attracted extensive interest as the wonder material, showing that line defects (LDs) occur widely at the interface between $v_{1/5}$ and $v_{1/6}$ boron sheets. Here, we study theoretically the electron transport through two-terminal disordered borophene nanoribbons (BNRs) with random distribution of LDs. Our results indicate that LDs strongly affect the electron transport properties of BNRs. Both $v_{1/5}$ and $v_{1/6}$ BNRs exhibit metallic behavior without any LD, in agreement with experiments. While in the presence of LDs, the overall electron transport ability is dramatically decreased, but some resonant peaks of conductance quantum are found in the transmission spectrum of any disordered BNR with arbitrary arrangement of LDs. These disordered BNRs exhibit metal-insulator transition with tunable transmission gap in the insulating regime. Furthermore, two evolution phenomena of resonant peaks are revealed for disordered BNRs with different widths. These results may help for understanding structure-property relationships and designing LD-based nanodevices.

npj Computational Materials (2022)8:131 ; https://doi.org/10.1038/s41524-022-00816-5

INTRODUCTION

Borophene, a monolayer of boron atoms, has attracted extensive attention as a prototype for exploring two-dimensional (2D) systems[1–3] since its successful synthesis by two independent groups[4,5] following theoretical predictions[6–12]. In contrast to other 2D materials[13–15], multiple borophene polymorphs including freestanding ones have been realized experimentally[16–22], which exhibit in-plane anisotropy and are tunable by ambient growth conditions. Of particular interest are the planar $v_{1/5}$ and $v_{1/6}$ boron sheets, which consist of (2,2) and (2,3) chains, respectively. Here, the indices a_n and a_w of (a_n,a_w) represent, respectively, the number of atoms in the narrow and wide rows of a single boron chain[23], as illustrated in Fig. 1a. These two sheets possess many intriguing attributes, such as superior mechanical strength and flexibility[24,25], conventional superconductivity[26–28], Dirac fermions[29–31], and ultrahigh thermal conductance[3,32].

On the other hand, line defects (LDs) exist in diverse 2D materials[33–38] and strongly affect their electronic, magnetic, optical, mechanical, and thermal properties[39–51]. Very recently, a specific LD at the interface between (2,2) and (2,3) chains has been widely reported in experiments[52–58], owing to higher structural stability of borophene in the presence of LDs[54,59]. Specifically, several distinct phases are synthesized from periodic self-assembly of LDs[52–54], implying that (2,2) and (2,3) chains function as building blocks to construct intriguing boron sheets. These LDs could considerably modulate the electronic properties of borophene[52,55,60] and improve its mechanical response[59], thus playing an important role in the discovery of exotic quantum phenomena and in device applications. Notice that the LDs in realistic borophene lack long-range order and structural disorder emerges simultaneously[52,54]. Until now, the LD-induced structural disorder has not yet been discussed and understanding this disorder may facilitate the elucidation of structure-property relationships.

In this paper, we study theoretically the electron transport through two-terminal borophene nanoribbons (BNRs) with random distribution of LDs by connecting to left and right semi-infinite $v_{1/5}$ BNRs. These BNRs, termed as disordered BNRs, are assembled from random arrangement of (2,2) and (2,3) chains in the central scattering region (CSR) and leads to LD-induced structural disorder, as shown in Fig. 1a. We find that both $v_{1/5}$ and $v_{1/6}$ BNRs exhibit metallic behavior, consistent with experiments[21–23,52]. Remarkably, although the overall electron transport ability is dramatically declined in the presence of LDs, some resonant peaks of conductance quantum appear in the transmission spectra of various disordered BNRs, regardless of inhomogeneous potential energies and hopping integrals, nanoribbon length, and LD distribution. By changing nanoribbon width, the disordered BNRs could present metal-insulator transition with tunable transmission gap in the insulating regime. Furthermore, two evolution phenomena of resonant peaks are revealed for disordered BNRs with different widths, showing that (i) all of the resonant peaks for odd width overlap perfectly with all those of two narrow BNRs and (ii) a specific resonant peak for width N_i reappears at various BNRs with width $N = a(N_i + 1) - 1$ and a an integer.

RESULTS

Tight-binding model

Electron transport through two-terminal disordered BNRs is simulated by the Hamiltonian[29,30]: $\mathcal{H} = \sum_i \varepsilon_i c_i^\dagger c_i - \sum_{\langle i,j \rangle} t_{ij} c_i^\dagger c_j$. Here, $c_i^\dagger$ (c_i) creates (annihilates) an electron at site i, ε_i is the potential energy, and t_{ij} is the nearest-neighbor hopping integral. In the numerical calculations, the parameters are set to $\varepsilon_i = 0$,

[1]Hunan Key Laboratory for Super-microstructure and Ultrafast Process, School of Physics and Electronics, Central South University, Changsha 410083, China. [2]School of Physical Science and Technology, Lanzhou University, Lanzhou 730000, China. [3]School of Sciences, Nantong University, Nantong 226019, China. [4]International Center for Quantum Materials, School of Physics, Peking University, Beijing 100871, China. [5]Collaborative Innovation Center of Quantum Matter, Beijing 100871, China. [6]CAS Center for Excellence in Topological Quantum Computation, University of Chinese Academy of Sciences, Beijing 100190, China. ✉email: aimin.guo@csu.edu.cn

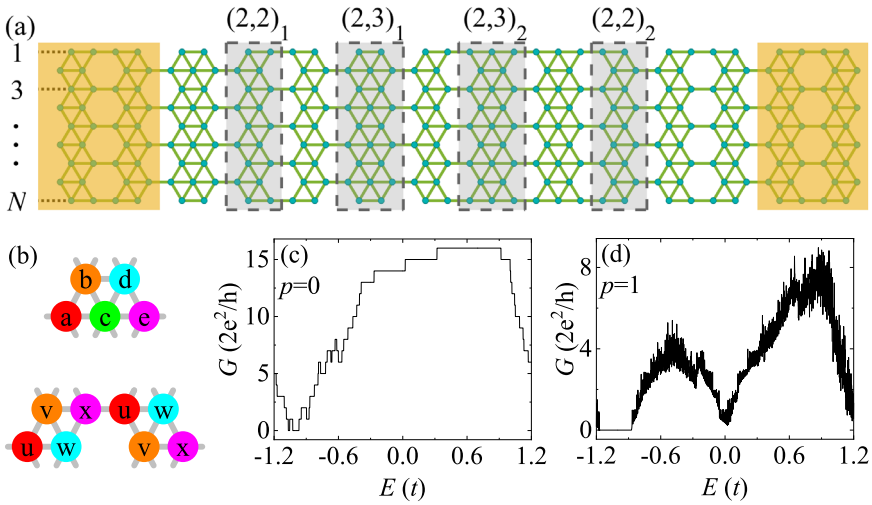

Fig. 1 Structure of a disordered BNR and electron transport along pure BNRs. a Schematics of a two-terminal disordered BNR coupled to left and right semi-infinite $v_{1/5}$ BNRs (yellow rectangles). This disordered BNR is assembled from random arrangement of (2,2) and (2,3) chains (gray rectangles) in the CSR, where a $(2,2)_j$ chain is followed randomly by a $(2,2)_{\bar{j}}$ or $(2,3)_{\bar{j}}$ one and a $(2,3)_j$ chain by a $(2,2)_j$ or $(2,3)_j$ one, with $\bar{j}=1$ (2) for $j=2$ (1). This leads to structural disorder induced by randomly distributed LDs and the disorder is characterized by the ratio p of (2,3) chains to all of the chains (length L). Here, the length is $L=10$ and the width defined as the number of rows is $N=9$. **b** The top panel shows the unit cell of $v_{1/6}$ borophene, which contains five boron atoms called as a, b, c, d, and e. The bottom panel plots the unit cell of $v_{1/5}$ one, which includes eight atoms labeled by u, v, w, and x. Energy-dependent conductance G for **c** a $v_{1/5}$ BNR with $p=0$ and **d** a $v_{1/6}$ BNR with $p=1$.

$t_{ij}=t=1$ (energy unit), and the nanoribbon length counted by all of the chains in the CSR to $L=2000$. The most disordered BNRs are considered in which half of the chains are (2,3) ones with $p=0.5$ and the results are averaged over 2500 disordered samples.

Pure BNRs

We first study the electron transport through pure BNRs with the CSR being a $v_{1/5}$ or $v_{1/6}$ BNR, as shown in Fig. 1c and d. It clearly appears that both $v_{1/5}$ and $v_{1/6}$ BNRs exhibit metallic behavior which is consistent with experiments[21–23,52], and their conductances are asymmetric about the line of $E=0$ owing to the electron-hole symmetry breaking. For the $v_{1/5}$ BNR, its transmission spectrum is characterized by many conductance plateaus quantized at integer multiples of G_0 as expected (Fig. 1c), because of the translational symmetry. By contrast, when the $v_{1/5}$ BNR is replaced by a $v_{1/6}$ one, the conductance declines and presents dramatic oscillating behavior instead of quantized plateaus (Fig. 1d), in accordance with first-principles calculations[60], because of LD-induced scattering at the CSR-lead interfaces.

Transmission peaks and important transport phenomena in disordered BNRs

Figure 2a and b show energy-dependent averaged conductance $\langle G\rangle$ and standard deviation δG, respectively, for disordered BNRs with different widths N. Here, $\delta G\equiv\sqrt{\langle G^2\rangle-\langle G\rangle^2}$. One can see that the electron transport through disordered BNRs is strongly suppressed as expected, due to Anderson localization caused by successive scattering from randomly distributed LDs. However, it is surprising that some transmission peaks of $\langle G\rangle=G_0$ are found in all these disordered BNRs and the peak number increases with N (Figs. 2a and 6b). In particular, the standard deviation at transmission-peak positions satisfies $\delta G\sim 0$ except for $E\sim 0.329t$ of $N=28$ and $E\sim 0.217t$ and $0.656t$ of $N=33$ (Fig. 2b), because the conductance contributed from neighboring transmission peak(s) fluctuates at these energies due to finite-size effects. We emphasize that $\delta G\sim 0$ at all these transmission-peak positions

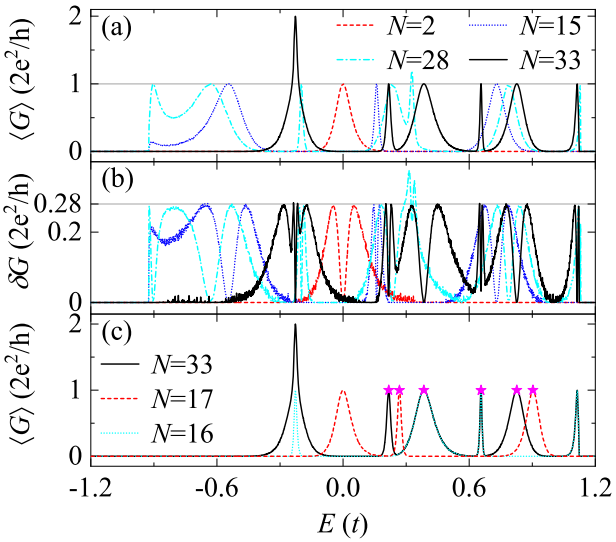

Fig. 2 Electron transport along disordered BNRs with different widths. Energy dependence of **a** averaged conductance $\langle G\rangle$ and **b** standard deviation δG for typical N. **c** $\langle G\rangle$ vs. E for three N. The gray lines in **a** and **b** denote the conductance quantum G_0 and $\delta G=0.28G_0$, respectively.

for longer disordered BNRs. All these transmission peaks are very robust, implying that they could be observed in any disordered BNR with arbitrary arrangement of LDs, as further discussed below. This result explains a recent experiment that delocalized states are measured in BNRs with LDs[55].

Besides, one can identify other important features. (i) The transport property of disordered BNRs strongly depends on N, ranging from metallic (see the red-dashed line in Fig. 2a) to insulating behavior (see the other lines in Fig. 2a). This indicates the width-driven metal-insulator transition in disordered BNRs. And the transmission gap is tunable in the insulating regime by

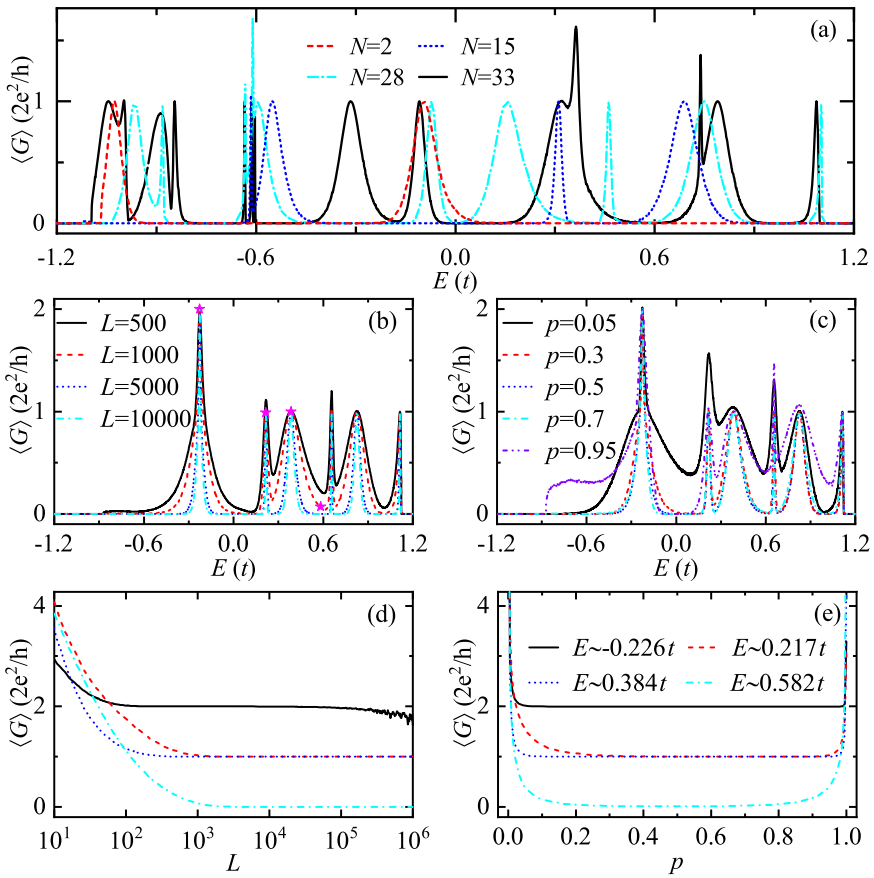

Fig. 3 Electron transport along disordered BNRs by considering inhomogeneous potential energies ε_i and hopping integrals t_{ij}, different lengths L, and ratios p. **a** $\langle G\rangle$ vs E for different N with inhomogeneous ε_i and t_{ij}. All these inhomogeneous model parameters are determined by the number of adjacent atoms[29,30], i.e., $\varepsilon_a = \varepsilon_e = \varepsilon_u = \varepsilon_x = -0.098t$, $\varepsilon_b = \varepsilon_d = \varepsilon_v = \varepsilon_w = 0.029t$, $\varepsilon_c = 0.4225t$, $t_{ab} = t_{de} = t_{uv} = t_{uw} = t_{vx} = t_{wx} = 1.02t$, $t_{ac} = t_{ce} = 0.895t$, $t_{ae} = t_{ax} = t_{eu} = t_{ux} = 1.06t$, $t_{bc} = t_{cd} = 0.92t$, and $t_{bd} = t_{vw} = 0.955t$. $\langle G\rangle$ vs E for **b** different L with $p = 0.5$ and for **c** typical p with $L = 2000$. **d** $\langle G\rangle$ vs L and **e** $\langle G\rangle$ vs p at the electron energies marked by the stars in **b**. The other model parameters in **b**, **c** are the same as Fig. 2a and $N = 33$.

varying N, which is similar to graphene nanoribbons[61–63] and facilitates band-gap engineering of BNRs. (ii) The transmission peaks, characterized by full width at half maximum (FWHM), are mainly categorized into narrow and wide peaks separated by about $0.06t$ FWHM (Figs. 2a and 6b). (iii) Every transmission peak corresponds to two peaks in the curve of δG-E (Fig. 2b). Remarkably, the maximum of all these peaks satisfies $\delta G \sim 0.28G_0$ (see the gray-solid line in Fig. 2b), which is close to $\sqrt{1/12}G_0$ reported in disordered graphene nanoribbons[64–66]. (iv) Some transmission peaks can even achieve $2G_0$ (see the black-solid line in Fig. 2a), because of almost perfect superposition of two neighboring transmission peaks, as seen from the four-peak structure around $E \sim -0.226t$ in Fig. 2b.

Robustness of transmission peaks in disordered BNRs

To demonstrate the robustness of transmission peaks, we study the electron transport along disordered BNRs by considering inhomogeneous potential energies ε_i and hopping integrals t_{ij}, different nanoribbon lengths L, and ratios p. Figure 3a shows $\langle G\rangle$ vs. E for disordered BNRs with inhomogeneous ε_i and t_{ij}, the values of which are determined by the number of neighboring boron atoms[29,30]. One can see that several transmission peaks of $\langle G\rangle = G_0$ are observed in the energy spectra of all these disordered BNRs with different N and the peak number increases with N.

Figure 3b plots $\langle G\rangle$ vs E with the length ranging from $L = 500$ to 10^4. Here, the width is $N = 33$ and the results are calculated from $5 \times 10^6/L$ disordered samples. It is clear that several transmission peaks are found in all these disordered BNRs and their FWHM depends on L. The FWHM is large for short disordered BNRs and will be progressively reduced by increasing L as expected, because the number of randomly distributed LDs is increased and gives rise to the enhancement of Anderson localization caused by continuous scattering from these LDs. However, all these peaks are very robust against the number and distribution of LDs, as further illustrated in Fig. 3d which shows $\langle G\rangle$ vs L at typical transmission-peak positions marked by the stars in Fig. 3b. With increasing L, $\langle G\rangle$ at the transmission-peak positions of $E \sim 0.217t$ and $0.384t$ declines firstly and then saturates at G_0 in the large length limit (see the red-dashed and blue-dotted lines in Fig. 3d). Similar behavior can also be observed at the peak position of $E \sim -0.226t$, but $\langle G\rangle$ achieves $2G_0$ for $10^2 < L < 10^5$ and is slightly decreased by further increasing L (see the black-solid line in Fig. 3d). This indicates that two transmission peaks almost overlap at $E \sim -0.226t$ and will be gradually separated from each other in the large length limit. In sharp contrast, $\langle G\rangle$ drops to zero when E deviates from the peak positions (see the cyan-dash-dotted line in Fig. 3d).

Figure 3c and e plot $\langle G\rangle$ vs E for typical p and $\langle G\rangle$ vs p at several E, respectively, by fixing $N = 33$ and $L = 2000$. One can see from Fig. 3c that all of the transmission peaks remain and the FWHM also depends on p. In the relatively low p regime, the FWHM decreases with p (see the black-solid, red-dashed, and blue-dotted

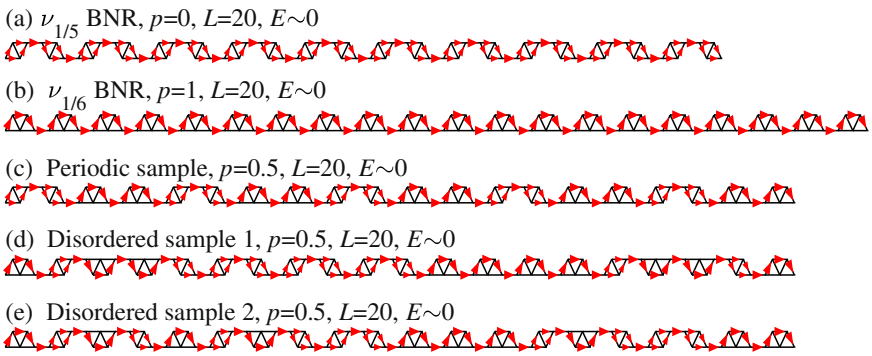

Fig. 4 Spatial distributions of bond currents at the resonant energy of $E \sim 0$ for different BNRs with various arrangement of (2,2) and (2,3) chains in the CSR. The top two panels refer to (**a**) a $\nu_{1/5}$ BNR and (**b**) a $\nu_{1/6}$ one, the middle panel (**c**) to a periodic BNR with $p = 0.5$, and the bottom panels (**d**) and (**e**) to two disordered samples with $p = 0.5$. Here, the width is $N = 2$, the length is $L = 20$, and the size of the arrows is proportional to the magnitude of bond currents.

lines in Fig. 3c); whereas in the high p regime, the FWHM usually increases with p (see the blue-dotted, cyan-dash-dotted, and violet-dash-dot-dotted lines in Fig. 3c). This nonmonotonic phenomenon can be understood from the aforementioned LD-induced Anderson localization. Notice that the number of randomly distributed LDs increases with p for $p < 0.5$ and decreases with p for $p > 0.5$. In other words, the situation of $p = 0.5$ corresponds to the most disordered BNRs and the disorder strength characterized by p becomes larger when p is closer to 0.5, giving rise to nonmonotonic dependence of the FWHM on p. Similar behavior can also be observed in the curves of $\langle G\rangle$-p that $\langle G\rangle$ decreases (increases) quickly with p in the extremely low (high) p regime (Fig. 3e). This can be traced back to the fact that the wave functions are very sensitive to LDs once they are introduced in the CSR and leads to dramatic modulation of the electron transport ability. However, all these peaks are very robust against LDs in this situation. For $E \sim 0.217t$ ($0.384t$), $\langle G\rangle$ reaches G_0 in a wide range of $0.17 < p < 0.97$ ($0.04 < p < 0.98$) (see the red-dashed and blue-dotted lines in Fig. 3e), while for $E \sim -0.226t$ $\langle G\rangle$ saturates at $2G_0$ in the range of $0.03 < p < 0.99$ (see the black-solid line in Fig. 3e). By contrast, $\langle G\rangle$ is decreased to zero when E situates away from the peak positions (see the cyan-dash-dotted line in Fig. 3e). Therefore, we conclude that the transmission peaks are very robust and could be detected in any disordered BNR with arbitrary arrangement of LDs, thus allowing for direct accessibility in experiments.

Physical origin of transmission peaks in disordered BNRs

To elucidate the physical origin of transmission peaks in disordered BNRs, we calculate bond currents of both periodic and disordered BNRs, and consider $N = 2$ as an example. The bond currents flowing from the lth chain to the $l+1$th one read[67–69]: $\mathbf{I}_l = (-2e/h)\int[\mathbf{H}_{l,l+1}\mathbf{G}^<_{l+1,l}(\xi) - \mathbf{H}_{l+1,l}\mathbf{G}^<_{l,l+1}(\xi)]d\xi$, where $\mathbf{G}^<_{l,l+1}$ is the interchain lesser Green's function. Figure 4a and b plot the spatial distributions of bond currents at the peak position of $E \sim 0$ for $\nu_{1/5}$ and $\nu_{1/6}$ BNRs, respectively, with $L = 20$. For the $\nu_{1/5}$ BNR, the current always flows along the outer edges of each (2,2) chain and its spatial distributions remain unchanged for the lth chain (Fig. 4a). While for the $\nu_{1/6}$ BNR, the current flows along the armchair edges within each (2,3) chain and the spatial distributions are independent of l as well (Fig. 4b). We then calculate the spatial distributions of bond currents at $E \sim 0$ for various BNRs with diverse arrangement of (2,2) and (2,3) chains in the CSR, as illustrated in Fig. 4c–e. We find that both spatial distributions and magnitude of bond currents within any (2,2) or (2,3) chain of all these BNRs, in the presence of LDs, are the same as those of $\nu_{1/5}$ and $\nu_{1/6}$ BNRs. In other words, the electrons at the peak positions will not be reflected by LDs and can thus propagate through any disordered BNR dissipationlessly.

To further understand the mechanism of transmission peaks, we study the electron transport through $\nu_{1/5}$ and $\nu_{1/6}$ BNRs with different L, and also take $N = 2$ as an example (Supplementary Fig. 1). It is clear that these transmission peaks originate from resonant tunneling, where some resonant energies remain unchanged for $\nu_{1/6}$ BNRs with different L and the others change with L. Therefore, the electrons with invariant resonant energies cannot be reflected by LDs, leading to resonant peaks in disordered BNRs.

Evolution phenomenon (EP) I

We then focus on the evolution of resonant peaks in disordered BNRs with various N. Figure 2c shows $\langle G\rangle$ vs E for disordered BNRs with three N. It clearly appears that some resonant peaks for $N = 33$ are superimposed on all those for $N = 16$, while the remaining ones will overlap with all those for $N = 17$ by properly moving peak positions. This phenomenon can also be observed in other disordered BNRs with, e.g., $N = 5$, 11, 13, and 27 (Supplementary Fig. 2). Therefore, we conclude that all of the resonant peaks of disordered BNRs with odd width N_o could be assembled from the ones with $N = (N_o - 1)/2$ and $(N_o + 1)/2$, namely, EP I.

To elucidate the underlying physics of EP I, Fig. 5 plots the spatial distributions of averaged interchain currents $\langle I_l(n)\rangle$ at typical resonant energies shown in Fig. 2c. It is clear that all of the $\langle I_l(n)\rangle$ exhibit rather uniform fringe patterns and are independent of l albeit the existence of randomly distributed LDs, manifesting delocalized states in various disordered BNRs. And green fringes denote transmission channels with finite $\langle I_l(n)\rangle$, whose number and location depend on E.

Since the spatial inversion symmetry with respect to the row of $n = (N+1)/2$ is preserved for disordered BNRs with odd N (Fig. 1a), the corresponding $\langle I_l(n)\rangle$ possess mirror symmetry (Fig. 5a and d–h) and can be divided into two cases according to the parity of wave functions. (i) The $\langle I_l(n)\rangle$ at $n = 17$ are zero for $N = 33$ (Fig. 5a and d), corresponding to odd wave functions whose electron densities are zero along the symmetric row of $n = 17$. In this situation, the top segment from $n = 1$ to 16 and the bottom one from $n = 18$ to 33, separated by this symmetric row, are independent of each other. Consequently, the transmission channels of the top/bottom segment for $N = 33$ are the same as those for $N = 16$ (Fig. 5a–d), giving rise to completely identical resonant peaks at the same E of these disordered BNRs. (ii) Contrarily, the $\langle I_l(n)\rangle$ are finite at $n = 17$ (Fig. 5e and h), which refers to even wave functions with nonzero electron densities along the symmetric row. Interestingly, the transmission channels of the top/bottom segment for $N = 33$ are also identical to those

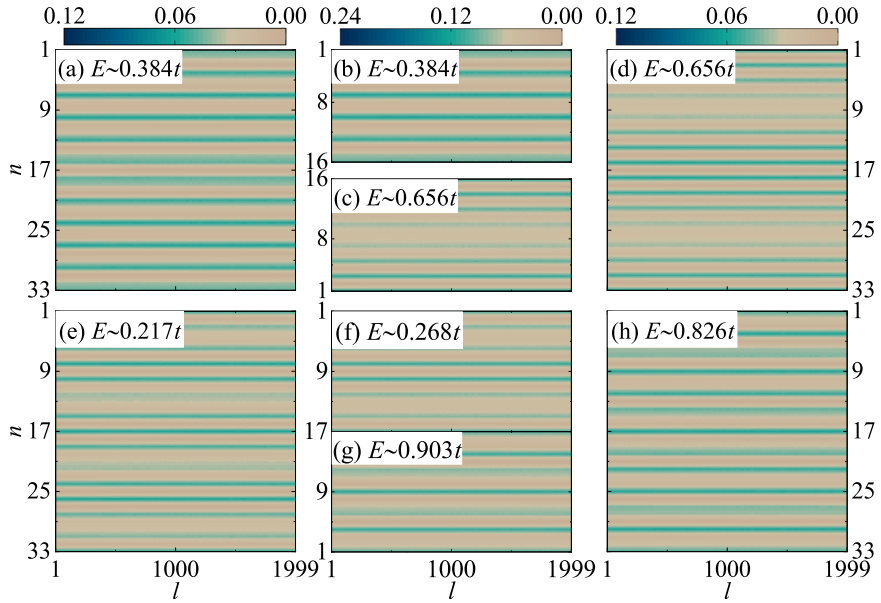

Fig. 5 Spatial distributions of averaged interchain currents $\langle I_l(n)\rangle$ of disordered BNRs at the resonant energies marked by the stars in Fig. 2c. 2D plots of $\langle I_l(n)\rangle$ vs chain index l and row index n for $N = 33$ at (**a**) $E \sim 0.384t$, (**d**) $E \sim 0.656t$, (**e**) $E \sim 0.217t$, and (**h**) $E \sim 0.826t$, for $N = 16$ at (**b**) $E \sim 0.384t$ and (**c**) $E \sim 0.656t$, and for $N = 17$ at (**f**) $E \sim 0.268t$ and (**g**) $E \sim 0.903t$.

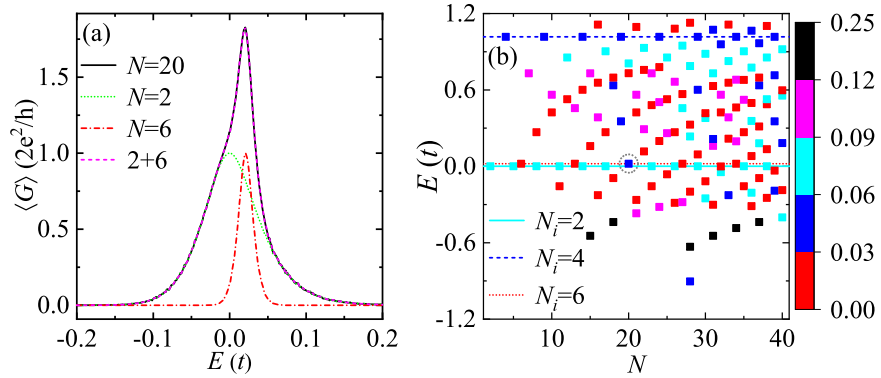

Fig. 6 Evolution of resonant peaks in disordered BNRs with different widths. a $\langle G\rangle$ vs. E around a peak for three N. The magenta-dashed line represents the sum of $\langle G\rangle$ for $N = 2$ and 6. **b** A 2D plot of FWHM for all of the peaks vs N and E. The cyan-solid, blue-dashed, and red-dotted lines display the evolution of three peaks initially appeared in disordered BNRs with width $N_i = 2$, 4, and 6, respectively.

for $N = 17$ albeit distinct magnitude of $\langle I_l(n)\rangle$ at the nth row (Fig. 5e–h). Correspondingly, the disordered BNRs with $N = 17$ and 33 possess identical resonant peaks but at different resonant energies, owing to the interference effect at the symmetric row. By contrast, the spatial inversion symmetry is destroyed for disordered BNRs with even N and the parity of wave functions disappears simultaneously, leading to the absence of EP I for even N.

EP II

Figure 6a shows $\langle G\rangle$ vs. E around a transmission peak for three disordered BNRs, where the magenta-dashed line represents the sum of $\langle G\rangle$ for $N = 2$ and 6. One can see that the peak at $E \sim 0.021t$ for $N = 20$ overlaps perfectly with the superposition of two neighboring peaks for $N = 2$ and 6, as seen from the black-solid and magenta-dashed lines in Fig. 6a. This indicates that a transmission peak of wide disordered BNRs could be evolved from narrow ones.

To further elucidate the above phenomenon, Fig. 6b displays a 2D plot of FWHM for all of the peaks as functions of N and E. It is clear that the number of squares increases with N and some disordered BNRs possess peculiar resonant peaks with FWHM exceeding $0.12t$ (see the leftmost peak for $N = 15$ in Fig. 2a and the black squares in Fig. 6b). In particular, completely identical resonant peaks are observed at $E \sim 0$ for $N = 2$, 5, 8,..., at $E \sim 1.017t$ for $N = 4$, 9, 14,..., and at $E \sim 0.021t$ for $N = 6$, 13,... (see the cyan-solid, blue-dashed, and red-dotted lines in Fig. 6b). Therefore, we infer that a resonant peak, firstly emerged in a disordered BNR with $N = N_i$, will reappear at the same E of various BNRs with $N = \alpha(N_i + 1) - 1$, where α is an integer and $N_i + 1$ the period. This characteristic is named as EP II, which compensates EP I. Notice that the peak at $E \sim 0.021t$ for $N = 3 \times 7 - 1 = 20$ deviates from EP II (see the surrounded blue square in Fig. 6b), because of finite-size effects. By increasing L, this transmission peak is split into two peaks at $E \sim 0$ and $0.021t$ (Fig. 6a). Consequently, this surrounded square will be evolved into a cyan (red) square on the cyan-solid (red-dashed) line and EP II holds.

To gain insights into EP II, we consider a disordered BNR with $N = \alpha(N_i + 1) - 1$. According to its spatial structure, this disordered sample could be divided into α basic BNRs with width N_i,

where the mth BNR includes the rows from $n = m_i - N_i$ to $m_i - 1$ and is separated from the m+1th one by the m_ith row, with $0 < m < a$ and $m_i = m(N_i + 1)$. For instance, the BNR with $N = 9$ can be divided into two basic BNRs with $N_i = 4$, which are separated by the fifth row (Fig. 1a). The Hamiltonian $\mathbf{H}_c$ of this disordered BNR with width N can then be partitioned as:

$$\mathbf{H}_c = \begin{bmatrix} \mathbf{H}_1 & \mathbf{A}_{11} & 0 & \cdots & 0 \\ \mathbf{A}_{11}^\dagger & \mathbf{R}_1 & \mathbf{A}_{21} & \ddots & \vdots \\ 0 & \mathbf{A}_{21}^\dagger & \mathbf{H}_2 & \ddots & 0 \\ \vdots & \ddots & \ddots & \ddots & \mathbf{A}_{a,a-1} \\ 0 & \cdots & 0 & \mathbf{A}_{a,a-1}^\dagger & \mathbf{H}_a \end{bmatrix} \quad (1)$$

where $\mathbf{H}_m$ and $\mathbf{R}_m$ are the sub-Hamiltonians of the mth basic BNR and the m_ith row, respectively, and $\mathbf{A}_{mn}$ the hopping matrix from the m_ith row to the mth BNR when $n = m$ and from the mth BNR to the $m_i - 1$th row when $n = m - 1$. Since the mth and $m + 1$th BNRs are mirror images about the m_ith row, the eigenstates of $\mathbf{H}_m$ and $\mathbf{H}_{m+1}$ are the same with identical eigenenergies, and the hopping matrices satisfy $\mathbf{A}_{m+1,m} = \mathbf{A}_{m,m}^\dagger$. Assuming the resonant state of the mth basic BNR is described by the Schrödinger equation of $\mathbf{H}_m|\mathbf{\Phi}_0\rangle = E_r|\mathbf{\Phi}_0\rangle$, with $|\mathbf{\Phi}_0\rangle$ the wave function and E_r the resonant energy, the wave function $|\mathbf{\Psi}\rangle$ of $\mathbf{H}_c$ can then be constructed as:

$$|\mathbf{\Psi}\rangle = \sqrt{a}/a(|\mathbf{\Phi}_0\rangle, 0, -|\mathbf{\Phi}_0\rangle, ..., (-1)^{a-1}|\mathbf{\Phi}_0\rangle)^{\mathrm{T}}. \quad (2)$$

Substituting Equations (1) and (2) into the Schrödinger equation, one obtains $\mathbf{H}_c|\mathbf{\Psi}\rangle = E_r|\mathbf{\Psi}\rangle$ straightforwardly. Thus, disordered BNRs with $N = a(N_i + 1) - 1$ possess a completely identical resonant peak for different a. These results are further confirmed by the numerical results of bond currents (Supplementary Fig. 3).

DISCUSSION

In summary, the electron transport along disordered BNRs with random distribution of LDs is investigated. Our results indicate that although the overall electron transport efficiency is strongly declined, some resonant peaks are observed in the transmission spectra and leads to delocalized states in various disordered BNRs. These disordered BNRs could exhibit metal-insulator transition by varying nanoribbon width with tunable transmission gap in the insulating regime. Besides, the evolution of resonant peaks in disordered BNRs with different widths is explored, which is related to the spatial inversion symmetry.

METHODS

According to the Landauer-Büttiker formula, the conductance is expressed as $G = G_0\mathrm{Tr}[\mathbf{\Gamma}_L\mathbf{G}^r\mathbf{\Gamma}_R\mathbf{G}^a]$. The conductance quantum $G_0 = 2e^2/h$, the Green's function $\mathbf{G}^r(E) = [\mathbf{G}^a(E)]^\dagger = [E\mathbf{I} - \mathbf{H}_c - \mathbf{\Sigma}_L^r - \mathbf{\Sigma}_R^r]^{-1}$, and the linewidth function $\mathbf{\Gamma}_{L/R} = i(\mathbf{\Sigma}_{L/R}^r - \mathbf{\Sigma}_{L/R}^a)$, with E the electron energy, $\mathbf{H}_c$ the CSR Hamiltonian, and $\mathbf{\Sigma}_{L/R}^r$ the retarded self-energy due to the coupling to the left/right semi-infinite $v_{1/5}$ BNR[70,71].

As seen from Fig. 1a, a disordered BNR with width N can alternatively be divided into $N/2$ ($(N-1)/2$) basic BNRs for even (odd) N. The width of this basic BNR is $N_i = 2$, and the mth basic BNR includes the $2m-1$th and $2m$th rows. Then, the Hamiltonian $\mathbf{H}_c$ of this disordered BNR with width N can be partitioned as:

$$\mathbf{H}_c = \begin{bmatrix} \mathbf{H}_1 & \mathbf{A}_{11} & 0 & \cdots \\ \mathbf{A}_{11}^\dagger & \mathbf{H}_1 & \mathbf{A}_{11} & \ddots \\ 0 & \mathbf{A}_{11}^\dagger & \mathbf{H}_1 & \ddots \\ \vdots & \ddots & \ddots & \ddots \end{bmatrix}, \quad (3)$$

where $\mathbf{H}_1$ is the sub-Hamiltonian of the basic BNR and $\mathbf{A}_{11}$ is the hopping matrix from the $m + 1$th basic BNR to the mth one. We emphasize that $\mathbf{H}_c$ in Equations (1) and (3) is identical to each other but with different block matrices.

As the basic BNR can be further divided into (2,2) and (2,3) chains with width $N_i = 2$, $\mathbf{H}_1$ can be expressed as:

$$\mathbf{H}_1 = \begin{bmatrix} \mathbf{h}_1 & \mathbf{h}_{12} & 0 & \cdots & 0 \\ \mathbf{h}_{12}^\dagger & \mathbf{h}_2 & \mathbf{h}_{23} & \ddots & \vdots \\ 0 & \mathbf{h}_{23}^\dagger & \mathbf{h}_3 & \ddots & 0 \\ \vdots & \ddots & \ddots & \ddots & \mathbf{h}_{L-1,L} \\ 0 & \cdots & 0 & \mathbf{h}_{L-1,L}^\dagger & \mathbf{h}_L \end{bmatrix}. \quad (4)$$

Here, $\mathbf{h}_l$ is the sub-Hamiltonian of the lth isolated chain and $\mathbf{h}_{l,l+1}$ is the hopping matrix between two neighboring chains. When the lth chain is (2,2) one, $\mathbf{h}_l$ reads

$$\mathbf{h}_l = \mathbf{h}_{(2,2)} = \begin{bmatrix} \varepsilon_u & t_{uv} & t_{uw} & 0 \\ t_{uv}^* & \varepsilon_v & t_{vw} & t_{vx} \\ t_{uw}^* & t_{vw}^* & \varepsilon_w & t_{wx} \\ 0 & t_{vx}^* & t_{wx}^* & \varepsilon_x \end{bmatrix}. \quad (5)$$

When the lth chain is (2,3) one, $\mathbf{h}_l$ reads

$$\mathbf{h}_l = \mathbf{h}_{(2,3)} = \begin{bmatrix} \varepsilon_a & t_{ab} & t_{ac} & 0 & 0 \\ t_{ab}^* & \varepsilon_b & t_{bc} & t_{bd} & 0 \\ t_{ac}^* & t_{bc}^* & \varepsilon_c & t_{cd} & t_{ce} \\ 0 & t_{bd}^* & t_{cd}^* & \varepsilon_d & t_{de} \\ 0 & 0 & t_{ce}^* & t_{de}^* & \varepsilon_e \end{bmatrix}. \quad (6)$$

The sub-Hamiltonian $\mathbf{h}_{(2,2)}$ corresponds to half of the unit cell of $v_{1/5}$ borophene (see the bottom panel of Fig. 1b), and $\mathbf{h}_{(2,3)}$ to the unit cell of $v_{1/6}$ borophene (see the top panel of Fig. 1b).

DATA AVAILABILITY

The data that support the findings of this study are available from the corresponding author upon reasonable request.

CODE AVAILABILITY

The codes that used to calculate the results of this study are available from the corresponding author upon reasonable request.

Received: 10 March 2022; Accepted: 29 May 2022;
Published online: 23 June 2022

REFERENCES

1. Zhang, Z., Penev, E. S. & Yakobson, B. I. Two-dimensional boron: structures, properties and applications. *Chem. Soc. Rev.* **46**, 6746–6763 (2017).
2. Mannix, A. J., Zhang, Z., Guisinger, N. P., Yakobson, B. I. & Hersam, M. C. Borophene as a prototype for synthetic 2D materials development. *Nat. Nanotechnol.* **13**, 444–450 (2018).
3. Li, D. et al. 2D boron sheets: structure, growth, and electronic and thermal transport properties. *Adv. Funct. Mater.* **30**, 1904349 (2020).
4. Mannix, A. J. et al. Synthesis of borophenes: anisotropic, two-dimensional boron polymorphs. *Science* **350**, 1513–1516 (2015).
5. Feng, B. et al. Experimental realization of two-dimensional boron sheets. *Nat. Chem.* **8**, 563–568 (2016).
6. Tang, H. & Ismail-Beigi, S. Novel precursors for boron nanotubes: the competition of two-center and three-center bonding in boron sheets. *Phys. Rev. Lett.* **99**, 115501 (2007).
7. Lau, K. C. & Pandey, R. Stability and electronic properties of atomistically-engineered 2D boron sheets. *J. Phys. Chem. C.* **111**, 2906–2912 (2007).
8. Yang, X., Ding, Y. & Ni, J. Ab initio prediction of stable boron sheets and boron nanotubes: structure, stability, and electronic properties. *Phys. Rev. B* **77**, 041402 (R) (2008).

9. Tang, H. & Ismail-Beigi, S. Self-doping in boron sheets from first principles: a route to structural design of metal boride nanostructures. *Phys. Rev. B* **80**, 134113 (2009).
10. Tang, H. & Ismail-Beigi, S. First-principles study of boron sheets and nanotubes. *Phys. Rev. B* **82**, 115412 (2010).
11. Penev, E. S., Bhowmick, S., Sadrzadeh, A. & Yakobson, B. I. Polymorphism of two-dimensional boron. *Nano Lett.* **12**, 2441–2445 (2012).
12. Wu, X., Dai, J., Zhao, Y., Zhuo, Z., Yang, J. & Zeng, X. C. Two-dimensional boron monolayer sheets. *ACS Nano* **6**, 7443–7453 (2012).
13. Das Sarma, S., Adam, S., Hwang, E. H. & Rossi, E. Electronic transport in two-dimensional graphene. *Rev. Mod. Phys.* **83**, 407 (2011).
14. Miró, P., Audiffred, M. & Heine, T. An atlas of two-dimensional materials. *Chem. Soc. Rev.* **43**, 6537–6554 (2014).
15. Barraza-Lopez, S., Fregoso, B. M., Villanova, J. W., Parkin, S. S. P. & Chang, K. Colloquium: physical properties of group-IV monochalcogenide monolayers. *Rev. Mod. Phys.* **93**, 011001 (2021).
16. Zhong, Q. et al. Metastable phases of 2D boron sheets on Ag(111). *J. Phys. Condens. Matter* **29**, 095002 (2017).
17. Li, W. et al. Experimental realization of honeycomb borophene. *Sci. Bull.* **63**, 282–286 (2018).
18. Wu, R. et al. Large-area single-crystal sheets of borophene on Cu(111) surfaces. *Nat. Nanotechnol.* **14**, 44–49 (2019).
19. Kiraly, B. et al. Borophene synthesis on Au(111). *ACS Nano* **13**, 3816–3822 (2019).
20. Vinogradov, N. A., Lyalin, A., Taketsugu, T., Vinogradov, A. S. & Preobrajenski, A. Single-phase borophene on Ir(111): formation, structure, and decoupling from the support. *ACS Nano* **13**, 14511–14518 (2019).
21. Ranjan, P. et al. Freestanding borophene and its hybrids. *Adv. Mater.* **31**, 1900353 (2019).
22. Feng, B. et al. Direct evidence of metallic bands in a monolayer boron sheet. *Phys. Rev. B* **94**, 041408(R) (2016).
23. Zhong, Q. et al. Synthesis of borophene nanoribbons on Ag(110) surface. *Phys. Rev. Mater.* **1**, 021001(R) (2017).
24. Zhang, Z. et al. Substrate-induced nanoscale undulations of borophene on silver. *Nano Lett.* **16**, 6622–6627 (2016).
25. Zhang, Z., Yang, Y., Penev, E. S. & Yakobson, B. I. Elasticity, flexibility, and ideal strength of borophenes. *Adv. Funct. Mater.* **27**, 1605059 (2017).
26. Penev, E. S., Kutana, A. & Yakobson, B. I. Can two-dimensional boron superconduct? *Nano Lett.* **16**, 2522–2526 (2016).
27. Gao, M., Li, Q.-Z., Yan, X.-W. & Wang, J. Prediction of phonon-mediated superconductivity in borophene. *Phys. Rev. B* **95**, 024505 (2017).
28. Zhao, Y., Zeng, S., Lian, C., Dai, Z., Meng, S. & Ni, J. Multigap anisotropic superconductivity in borophenes. *Phys. Rev. B* **98**, 134514 (2018).
29. Feng, B. et al. Dirac fermions in borophene. *Phys. Rev. Lett.* **118**, 096401 (2017).
30. Ezawa, M. Triplet fermions and Dirac fermions in borophene. *Phys. Rev. B* **96**, 035425 (2017).
31. Feng, B. et al. Discovery of 2D anisotropic Dirac cones. *Adv. Mater.* **30**, 1704025 (2018).
32. Zhou, H., Cai, Y., Zhang, G. & Zhang, Y.-W. Superior lattice thermal conductance of single-layer borophene. *npj 2D Mater. Appl.* **1**, 14 (2017).
33. Lahiri, J., Lin, Y., Bozkurt, P., Oleynik, I. I. & Batzill, M. An extended defect in graphene as a metallic wire. *Nat. Nanotechnol.* **5**, 326–329 (2010).
34. van der Zande, A. M. et al. Grains and grain boundaries in highly crystalline monolayer molybdenum disulphide. *Nat. Mater.* **12**, 554–561 (2013).
35. Najmaei, S. et al. Vapour phase growth and grain boundary structure of molybdenum disulphide atomic layers. *Nat. Mater.* **12**, 754–759 (2013).
36. Cretu, O., Lin, Y.-C. & Suenaga, K. Evidence for active atomic defects in monolayer hexagonal boron nitride: a new mechanism of plasticity in two-dimensional materials. *Nano Lett.* **14**, 1064–1068 (2014).
37. Liu, M. et al. Graphene-like nanoribbons periodically embedded with four- and eight-membered rings. *Nat. Commun.* **8**, 14924 (2017).
38. Pawlak, R., Drechsel, C., D'Astolfo, P., Kisiel, M., Meyer, E. & Cerda, J. I. Quantitative determination of atomic buckling of silicene by atomic force microscopy. *Proc. Natl. Acad. Sci. USA* **117**, 228–237 (2020).
39. Gunlycke, D. & White, C. T. Graphene valley filter using a line defect. *Phys. Rev. Lett.* **106**, 136806 (2011).
40. Kou, L., Tang, C., Guo, W. & Chen, C. Tunable magnetism in strained graphene with topological line defect. *ACS Nano.* **5**, 1012–1017 (2011).
41. Song, J., Liu, H., Jiang, H., Sun, Q.-f & Xie, X. C. One-dimensional quantum channel in a graphene line defect. *Phys. Rev. B* **86**, 085437 (2012).
42. Huang, H., Xu, Y., Zou, X., Wu, J. & Duan, W. Tuning thermal conduction via extended defects in graphene. *Phys. Rev. B* **87**, 205415 (2013).
43. Komsa, H.-P., Kurasch, S., Lehtinen, O., Kaiser, U. & Krasheninnikov, A. V. From point to extended defects in two-dimensional MoS_2: Evolution of atomic structure under electron irradiation. *Phys. Rev. B* **88**, 035301 (2013).
44. Phillips, M. & Mele, E. J. Zero modes on zero-angle grain boundaries in graphene. *Phys. Rev. B* **91**, 125404 (2015).
45. de Oliveira, J. B., de Oliveira, I. S. S., Padilha, J. E. & Miwa, R. H. Tunable magnetism and spin-polarized electronic transport in graphene mediated by molecular functionalization of extended defects. *Phys. Rev. B* **97**, 045107 (2018).
46. Rhim, J.-W., Bardarson, J. H. & Slager, R.-J. Unified bulk-boundary correspondence for band insulators. *Phys. Rev. B* **97**, 115143 (2018).
47. Li, X., Zhang, S., Huang, H., Hu, L., Liu, F. & Wang, Q. Unidirectional spin-orbit interaction induced by the line defect in monolayer transition metal dichalcogenides for high-performance devices. *Nano Lett.* **19**, 6005–6012 (2019).
48. Kähärä, T. & Koskinen, P. Rippling of two-dimensional materials by line defects. *Phys. Rev. B* **102**, 075433 (2020).
49. Kondrin, M. V., Lebed, Y. B. & Brazhkin, V. V. Extended defects in graphene and their contribution to the excess specific heat at high temperatures. *Phys. Rev. Lett.* **126**, 165501 (2021).
50. Hsieh, K. et al. Spontaneous time-reversal symmetry breaking at individual grain boundaries in graphene. *Phys. Rev. Lett.* **126**, 206803 (2021).
51. Wan, F., Wang, X., Guo, Y., Zhang, J., Wen, Z. & Li, Y. Role of line defect in the bandgap and transport properties of silicene nanoribbons. *Phys. Rev. B* **104**, 195413 (2021).
52. Liu, X., Zhang, Z., Wang, L., Yakobson, B. I. & Hersam, M. C. Intermixing and periodic self-assembly of borophene line defects. *Nat. Mater.* **17**, 783–788 (2018).
53. Liu, X., Wang, L., Li, S., Rahn, M. S., Yakobson, B. I. & Hersam, M. C. Geometric imaging of borophene polymorphs with functionalized probes. *Nat. Commun.* **10**, 1642 (2019).
54. Wang, Y. et al. Realization of regular-mixed quasi-1D borophene chains with long-range order. *Adv. Mater.* **32**, 2005128 (2020).
55. Kong, L. et al. One-dimensional nearly free electron states in borophene. *Nanoscale* **11**, 15605–15611 (2019).
56. Liu, L. et al. Borophene concentric superlattices via self-assembly of twin boundaries. *Nano Lett.* **20**, 1315–1321 (2020).
57. Li, Q. et al. Synthesis of borophane polymorphs through hydrogenation of borophene. *Science* **371**, 1143–1148 (2021).
58. Liu, X., Wang, L., Yakobson, B. I. & Hersam, M. C. Nanoscale probing of image-potential states and electron transfer doping in borophene polymorphs. *Nano Lett.* **21**, 1169–1174 (2021).
59. Xu, S.-G., He, C.-C., Zhao, Y.-J., Xu, H. & Yang, X.-B. Unconventional line defects engineering in two-dimensional boron monolayers. *Phys. Rev. Mater.* **5**, 044003 (2021).
60. Zeng, J. & Chen, K.-Q. Charge transport in borophene: role of intrinsic line defects. *J. Phys. Chem. C.* **123**, 6270–6275 (2019).
61. Ezawa, M. Peculiar width dependence of the electronic properties of carbon nanoribbons. *Phys. Rev. B* **73**, 045432 (2006).
62. Son, Y.-W., Cohen, M. L. & Louie, S. G. Energy gaps in graphene nanoribbons. *Phys. Rev. Lett.* **97**, 216803 (2006).
63. Han, M. Y., Özyilmaz, B., Zhang, Y. & Kim, P. Energy band-gap engineering of graphene nanoribbons. *Phys. Rev. Lett.* **98**, 206805 (2007).
64. Rycerz, A., Tworzydło, J. & Beenakker, C. W. J. Anomalously large conductance fluctuations in weakly disordered graphene. *Europhys. Lett.* **79**, 57003 (2007).
65. Abanin, D. A. & Levitov, L. S. Quantized transport in graphene p-n junctions in a magnetic field. *Science* **317**, 641–643 (2007).
66. Chen, J.-C., Zhang, H., Shen, S.-Q. & Sun, Q.-F. Dephasing effect on transport of a graphene p-n junction in a quantum Hall regime. *J. Phys. Condens. Matter* **23**, 495301 (2011).
67. Hu, P.-J. et al. Spin-dependent electron transport along hairpinlike DNA molecules. *Phys. Rev. B* **102**, 195406 (2020).
68. Cresti, A., Farchioni, R., Grosso, G. & Parravicini, G. P. Keldysh-Green function formalism for current profiles in mesoscopic systems. *Phys. Rev. B* **68**, 075306 (2003).
69. Lewenkopf, C. H. & Mucciolo, E. R. The recursive Green's function method for graphene. *J. Comput. Electron.* **12**, 203–231 (2013).
70. Lopez Sancho, M. P., Lopez Sancho, J. M. & Rubio, J. Quick iterative scheme for the calculation of transfer matrices: application to Mo(100). *J. Phys. F. Met. Phys.* **14**, 1205 (1984).
71. Lopez Sancho, M. P., Lopez Sancho, J. M. & Rubio, J. Highly convergent schemes for the calculation of bulk and surface Green functions. *J. Phys. F. Met. Phys.* **15**, 851 (1985).

ACKNOWLEDGEMENTS

This work is supported by the National Natural Science Foundation of China (Grants No. 11874428, No. 11874187, and No. 11921005), the National Key Research and Development Program of China (Grant No. 2017YFA0303301), and the High Performance Computing Center of Central South University.

AUTHOR CONTRIBUTIONS

A.-M.G. designed research. P.-J.H. performed research. P.-J.H., S.-X.W., A.-M.G., and Q.-F.S. analyzed the data. P.-J.H., S.-X.W., X.-F.C., Z.-R.L., T.-F.F., A.-M.G., H.X., and Q.-F.S. wrote the paper. P.-J.H. and S.-X.W. contributed equally.

COMPETING INTERESTS

The authors declare no competing interests.

ADDITIONAL INFORMATION

Supplementary information The online version contains supplementary material available at https://doi.org/10.1038/s41524-022-00816-5.

Correspondence and requests for materials should be addressed to Ai-Min Guo.

Reprints and permission information is available at http://www.nature.com/reprints

Publisher's note Springer Nature remains neutral with regard to jurisdictional claims in published maps and institutional affiliations.

Open Access This article is licensed under a Creative Commons Attribution 4.0 International License, which permits use, sharing, adaptation, distribution and reproduction in any medium or format, as long as you give appropriate credit to the original author(s) and the source, provide a link to the Creative Commons license, and indicate if changes were made. The images or other third party material in this article are included in the article's Creative Commons license, unless indicated otherwise in a credit line to the material. If material is not included in the article's Creative Commons license and your intended use is not permitted by statutory regulation or exceeds the permitted use, you will need to obtain permission directly from the copyright holder. To view a copy of this license, visit http://creativecommons.org/licenses/by/4.0/.

© The Author(s) 2022